Bioactive Materials 7 (2022) 26–38

Contents lists available at ScienceDirect

Bioactive Materials

journal homepage: www.sciencedirect.com/journal/bioactive-materials

# Surface treatment of 3D printed porous Ti6Al4V implants by ultraviolet photofunctionalization for improved osseointegration

Chuan Yin [a,1], Teng Zhang [b,1], Qingguang Wei [a], Hong Cai [a], Yan Cheng [c], Yun Tian [a], Huijie Leng [a], Caimei Wang [d], Shiqing Feng [b,**], Zhongjun Liu [a,*]

[a] Department of Orthopedics, Peking University Third Hospital, Beijing, 100191, People's Republic of China
[b] Department of Orthopedics, Qilu Hospital of Shandong University, Jinan, 250012, People's Republic of China
[c] Center for Biomedical Materials and Tissue Engineering, Academy for Advanced Interdisciplinary Studies, Peking University, Beijing, 100871, People's Republic of China
[d] Beijing AKEC Medical Company Ltd., Beijing, 102200, People's Republic of China

ARTICLE INFO

*Keywords:*
Three-dimensional-printed porous implants
UV photofunctionalization
Omnidirectional UV radiator
Osseointegration

ABSTRACT

Three-dimensional (3D)-printed porous Ti6Al4V implants play an important role in the reconstruction of bone defects. However, its osseointegration capacity needs to be further improved, and related methods are inadequate, especially lacking customized surface treatment technology. Consequently, we aimed to design an omnidirectional radiator based on ultraviolet (UV) photofunctionalization for the surface treatment of 3D-printed porous Ti6Al4V implants, and studied its osseointegration promotion effects *in vitro* and *in vivo*, while elucidating related mechanisms. Following UV treatment, the porous Ti6Al4V scaffolds exhibited significantly improved hydrophilicity, cytocompatibility, and alkaline phosphatase activity, while preserving their original mechanical properties. The increased osteointegration strength was further proven using a rabbit condyle defect model *in vivo*, in which UV treatment exhibited a high efficiency in the osteointegration enhancement of porous Ti6Al4V scaffolds by increasing bone ingrowth (BI), the bone-implant contact ratio (BICR), and the mineralized/osteoid bone ratio. The advantages of UV treatment for 3D-printed porous Ti6Al4V implants using the omnidirectional radiator in the study were as follows: 1) it can significantly improve the osseointegration capacity of porous titanium implants despite the blocking out of UV rays by the porous structure; 2) it can evenly treat the surface of porous implants while preserving their original topography or other morphological features; and 3) it is an easy-to-operate low-cost process, making it worthy of wide clinical application.

## 1. Introduction

The treatment of bone defects has been a challenge for orthopedists [1,2]. Globally, over 2.2 million bone graft surgeries are performed annually to reconstruct bone defects in orthopedics, neurosurgery, and dentistry [3]. A three-dimensional (3D)-printed porous Ti alloy implant was developed and proven to be advantageous in reconstructing bone defects, including accuracy in shape and size with no need for bone grafting, meeting the needs for patient-specific design and immediate stability [4,5]. Further, its porous features favor bone ingrowth [6,7] and avoid stress shielding [8,9] of the solid implant. However, owing to the bioinert nature of Ti6Al4V, osteoinduction of the 3D-printed porous implant surface is insufficient, the exposure of Ti6Al4V to air further reducing its bioactivity [10]. Hence, further improvements in the osteoinduction of 3D-printed porous Ti6Al4V is critical to broaden its range of applications, such as the treatment of bone defects in poor quality bone beds or infective bone defects.

To date, various methods have been developed to enhance the osseointegration of 3D-printed porous Ti6Al4V implants. One method is the incorporation of autologous skeletal stem cells or autogenous bone into porous implants [11,12]. However, taking autologous bone marrow from the iliac intraoperatively causes extra surgical trauma to patients. Other methods include surface modification by calcium phosphate-like

Peer review under responsibility of KeAi Communications Co., Ltd.
* Corresponding author.
** Corresponding author.
*E-mail address:* puthztlzj@163.com (Z. Liu).
[1] These authors contributed equally to this study.

https://doi.org/10.1016/j.bioactmat.2021.05.043
Received 15 May 2021; Received in revised form 25 May 2021; Accepted 25 May 2021
Available online 25 June 2021

**Abbreviations**

| | |
|---|---|
| ALP | alkaline phosphatase |
| 3D | three-dimensional |
| BI | bone ingrowth |
| BICR | bone-implant contact ratio |
| CAD | computer-aided design |
| CLSM | confocal laser scanning microscopy |
| DMEM | Dulbecco's modified Eagle's medium |
| EBM | electron beam melting |
| EDS | energy-dispersive X-ray spectrometer |
| FE-SEM | field emission scanning electron microscope |
| HU | hounsfield units |
| OM | osteogenic medium |
| PBS | phosphate buffered saline |
| rhBMP-2 | recombinant human bone morphogenic protein 2 |
| ROI | regions of interest |
| SEM | scanning electron microscope |
| UV | ultraviolet |
| XPS | X-ray photoelectron spectroscopy |
| micro-CT | micro-computed tomography |

implant contact by changing the biological and biochemical properties of titanium [17–19]. It has been reported that titanium surfaces undergo a significant decrease in osseointegration capability after processing, which is associated with the disappearance of hydrophilicity [20], the progressive contamination of hydrocarbons [21], and the electrostatic status change on titanium surfaces over time [22]. Long-preserved titanium surfaces could be recovered by UV treatment and showed even better biocompatibility than the freshly prepared surfaces—particularly in protein adsorption and osteoblast attachment, proliferation, differentiation, and mineralization, as well as the *in vivo* capability of osseointegration [23]. Photofunctionalization has been widely used in dentistry in recent years [24]; however, to date, UV treatment has not been attempted in 3D-printed porous Ti6Al4V implants, and the corresponding effects and related mechanisms are unknown. Moreover, there is no UV irradiation equipment specifically for 3D-printed porous Ti6Al4V implants currently available. As UV photofunctionalization is effective on various titanium surfaces without altering their original topography or other morphological features, we specially designed a device targeted at the UV treatment of 3D-printed porous Ti6Al4V implants for osseointegration improvement [17–23].

The advantages of UV functionalization for 3D-printed porous Ti6Al4V implants are as follows: first, the functionalization of UV light has little effect on the original topography or other morphological features of the porous implant itself, and the surface of the porous implant

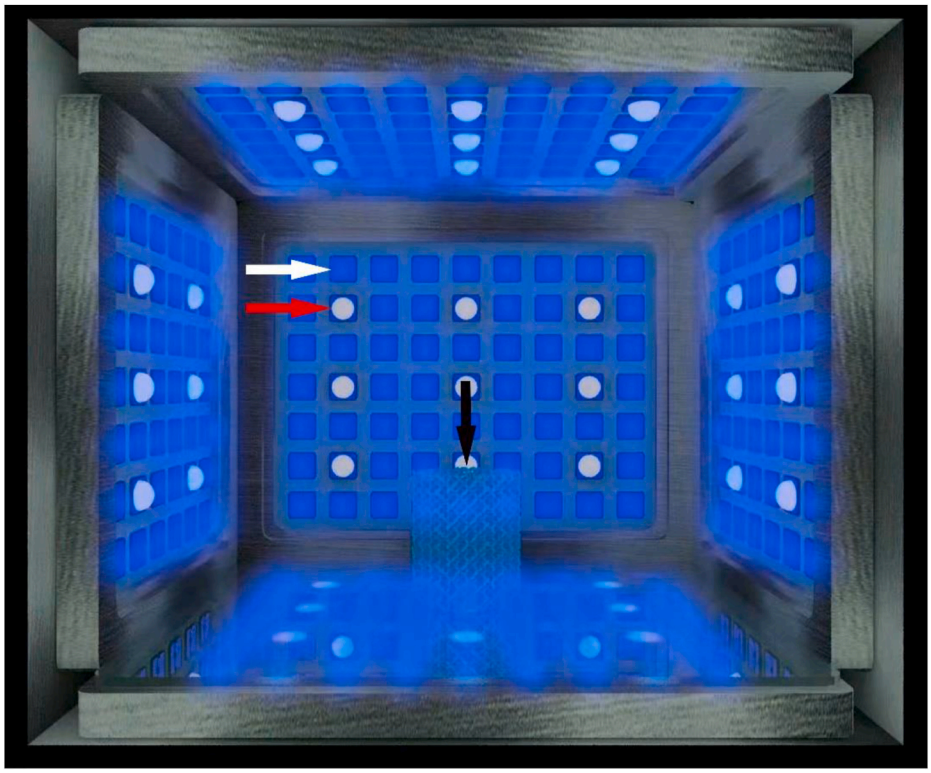

**Fig. 1.** The interior view of the omnidirectional UV radiator. The black arrow indicates the 3D printed porous Ti6Al4V scaffolds. The white arrow indicates the ultraviolet led bead of 270 nm. The red arrow indicates the ultraviolet led bead of 365 nm.

or biomolecule coatings [13–15], a complicated process with limited osseointegration enhancing effects. The combined use of exogenous recombinant human bone morphogenic protein 2 (rhBMP-2) with 3D-printed porous Ti6Al4V implants has also been attempted to improve osseointegration [16]. However, the rhBMP-2 product results in enormous additional fees for patients.

Photofunctionalization, which involves the use of ultraviolet (UV) treatment to modify titanium surfaces, has been shown to enhance bone-

is evenly treated. Second, UV functionalization can improve the performance of titanium metal in many respects, including anti-contamination [21], anti-bacterial [25] and anti-rust capabilities [26]. UV functionalization is also easy to operate, requiring less equipment and lower cost, making it worthy of wide clinical application. Considering the positive role of UV functionalization in osteointegration, we hypothesized that it may be a promising candidate for the realization of optimal designs, as mentioned above. In this study, we characterized

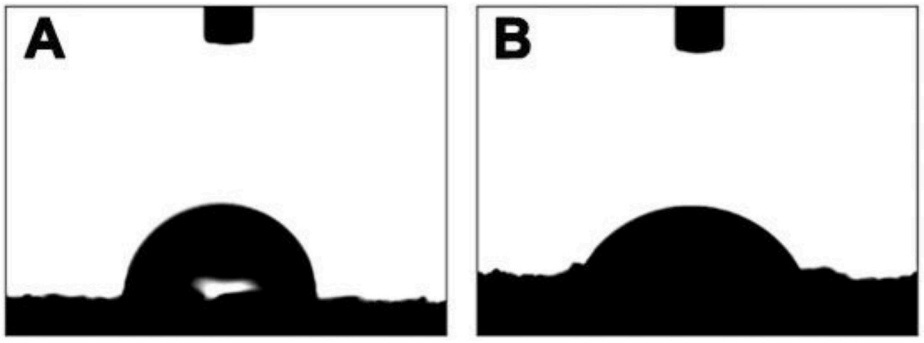


**Fig. 2.** Comparison of contact angles between GC **(A)** and GU **(B)** groups.

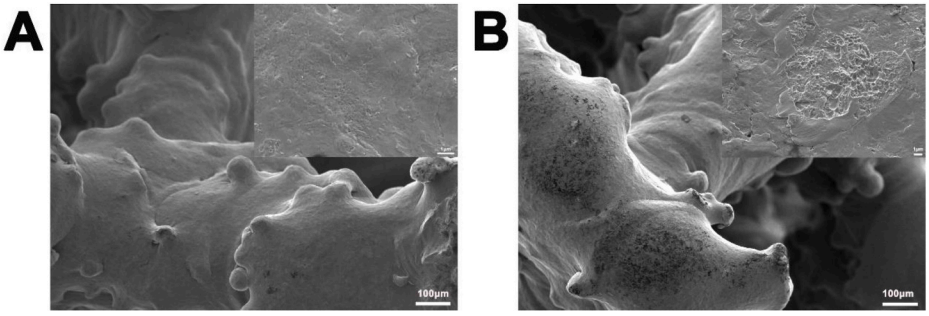


**Fig. 3.** SEM images ( × 100 and × 10000 magnification) of the surface landscapes of GC (A) and GU (B) scaffolds.

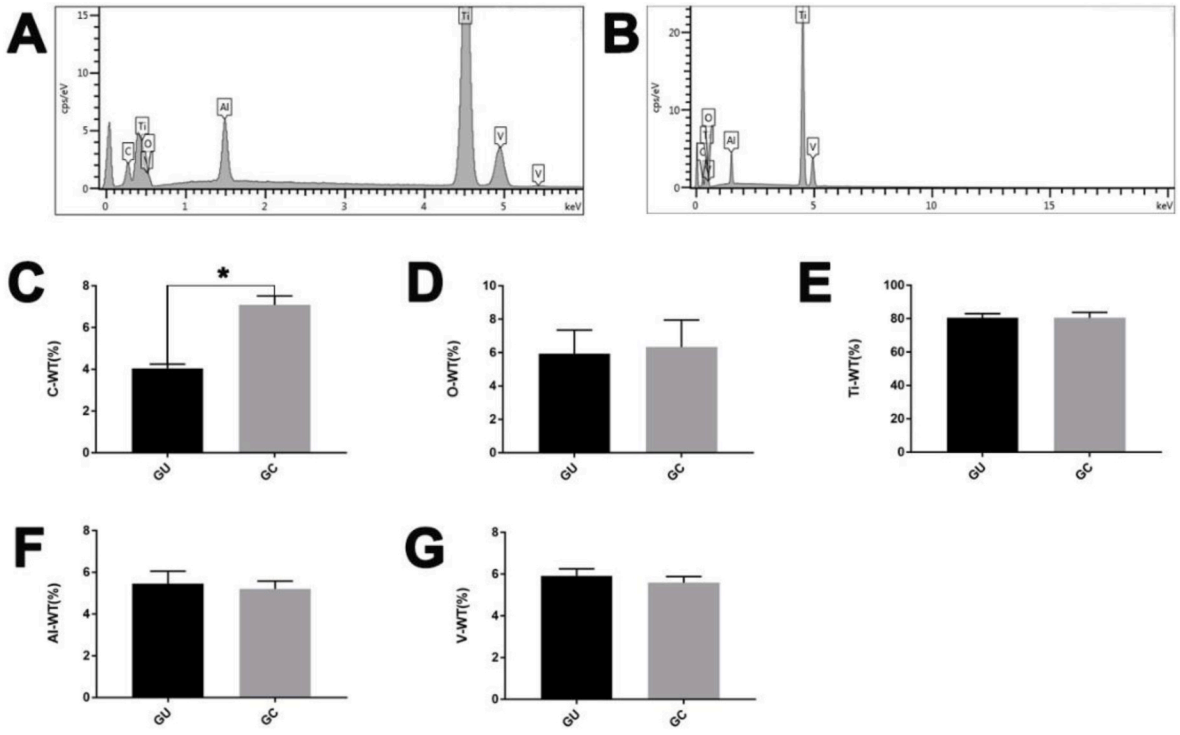


**Fig. 4.** Elementary composition characterized by EDS of GC **(A)** and GU **(B)** group. The atomic mass percentage of C **(C)**, O **(D)**, Ti **(E)**, Al **(F),** and V **(G)** elements on the inner surface of the GC and the GU group determined by EDS. The content of carbon (elemental C) on the inner surface of the GU group was significantly lower than that of the GC group (*P < 0.05), and there was no significant difference between the other elements.

and analyzed the 3D printed porous Ti6Al4V scaffold and investigated its effects on cell proliferation and osteoblast differentiation *in vitro*. We also validated the osseointegration of the scaffold in a rabbit bone defect model.

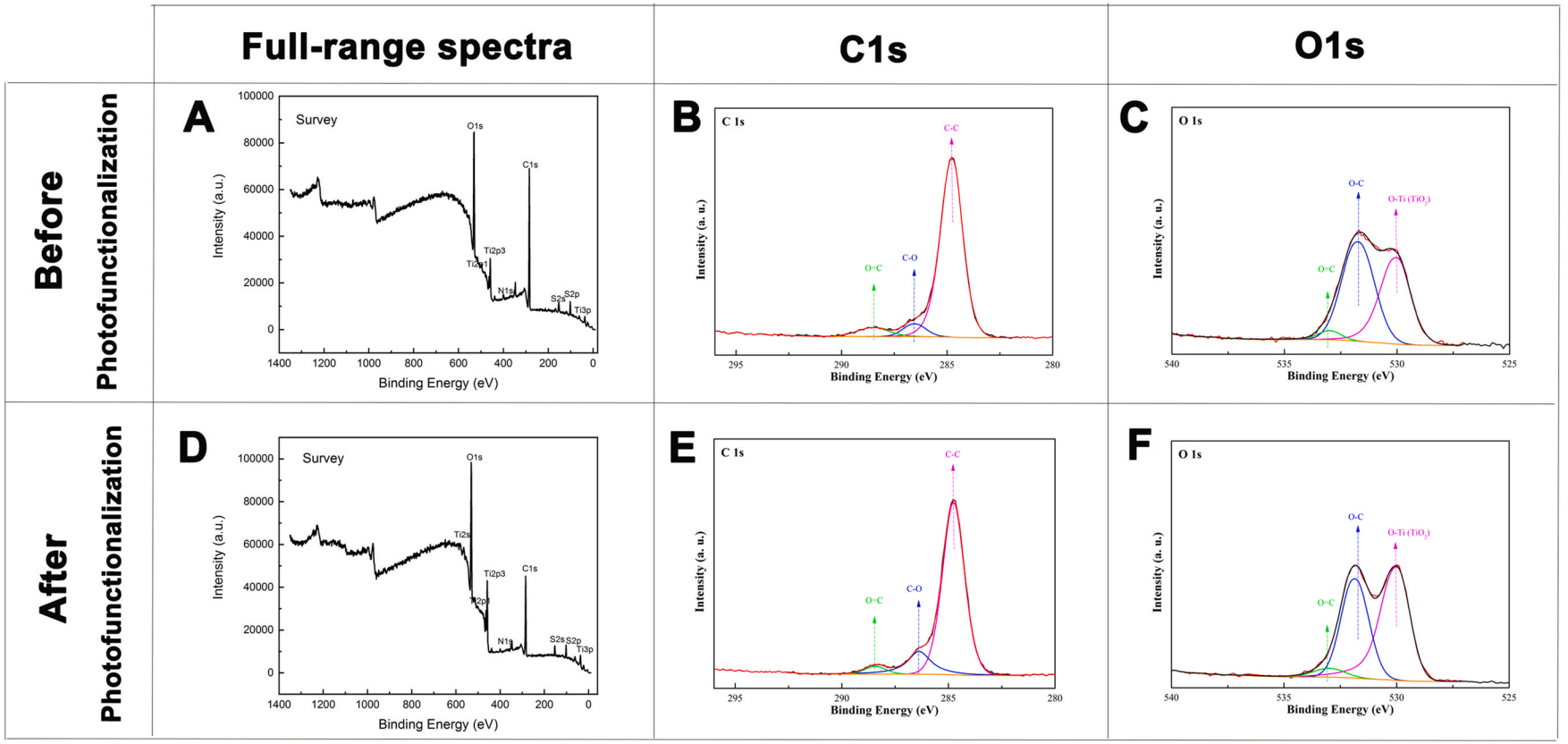


**Fig. 5.** Full spectrum of XPS of GC **(A)** and GU **(D)** group. Peak-differentiating and imitating of C element in GU group **(B)** and GC group **(E)**. **(F)**. Peak-differentiating and imitating of O element in GC group **(C) and** GU group **(F)**.

**Table 1**
Comparison of C elements in different chemical environments in the two groups.

| | GC (%) | GU (%) |
|---|---|---|
| C–C | 87.45 | 81.72 |
| C–O | 6.13 | 14.8 |
| C=O | 6.42 | 3.48 |

**Table 2**
Comparison of O elements in different chemical environments in the two groups.

| | GC (%) | GU (%) |
|---|---|---|
| O–Ti ($TiO_2$) | 44 | 53.9 |
| O–C | 51.92 | 41.4 |
| O=C | 4.08 | 4.69 |

## 2. Materials and methods

### 2.1. Sample preparation

The porous Ti6Al4V scaffolds used in this study were prepared using electron beam melting (EBM) additive manufacturing technology. Ti6Al4V scaffolds (diameter, 5 mm; length, 6 mm; pore size diameter, 400 μm; porosity, 73%) were created using computer-assisted design (CAD) software (Magics, Materialize, Belgium). This architecture was adopted because a previous study had demonstrated such pore size to be beneficial for the ingrowth of bone and vessels [14].

### 2.2. Omnidirectional UV radiator design and UV treatment

Considering the blocking of UV rays by the porous structure of the 3D-printed porous Ti6Al4V implants, UV led beads were installed in such a way as to create a device containing a (3 × 3 × 4 cm) irradiation cube, in which the values of radiation intensity were more than 2 MW/$cm^2$ (270 nm) and 30 MW/$cm^2$ (365 nm). These two intensities and wavelengths of UV light have been proven to be effective in improving osteointegration. The specially designed UV photofunctionalization device is called an omnidirectional radiator. The distance between each UV led bead being 5 mm. The led beads were evenly arranged to form a (3 × 3 × 4 $cm^3$) irradiation cube in which the scaffolds were irradiated, as shown in Fig. 1. The simulated test values of the radiation intensity in the space were more than 2 MW/$cm^2$ (270 nm) and 30 MW/$cm^2$ (365 nm). UV Hg-Vapor lamp [2mw/$cm^2$ ( 250 ± 20 nm ) and 0.1mw/$cm^2$ ( 360 ± 20 nm ) ] has been proved that it can be used as light source to promote osseointegration [29,30]. Moreover, the UV LED beads have been proved to be a good alternative light source to reduce the surface C contamination [31]. Therefore, we choose 270 nm and 365 nm UV LED beads as light sources, and their irradiation intensity meets or even exceeds the intensity requirements of the corresponding wavelength of the UV Hg-Vapor lamp. Meanwhile, the test of intensity by Tracepro70 (CHS) and the real measured value of optical power meter are all beyond 2 MW/$cm^2$ (270 nm) and 30 MW/$cm^2$ (365 nm). So they were chosen as the light sources. The vital design principles of the omnidirectional UV Radiator includes: 1) The irradiating energy at 270 nm is beyond 2 MW/$cm^2$, and at 365 nm is beyond 30 MW/$cm^2$; 2) Enough space for the implants. In brief, Before UV treatment, all samples were kept in dark place for 4 weeks to lose bioactivity as standard protocol [32]. then they were treated for 15 min by UV photofunctionalization and sealed, followed by high-pressure steam sterilization and drying within 24 h. For simplicity, hereafter, the group of the Ti6Al4V scaffolds treated using the omnidirectional UV radiator are denoted as GU, and the control group of the Ti6Al4V scaffolds without any treatment are denoted as GC.

### 2.3. Wettability measurements

The contact angle of the 3D printed titanium alloy (10 in each group) was measured and photographed using the session drop method, the angle being measured using the direct measurement method, after which statistical analysis was conducted.

### 2.4. Surface characterizations

After the treatment, a porous titanium alloy scaffold was cut from the middle using a diamond saw, and the surface morphology of the porous metal scaffold was analyzed using a field emission scanning electron microscope (FE-SEM: s-4800, Hitachi). Furthermore, an energy-dispersive X-ray spectrometer (EDS: DX-4, Philips, the Netherlands) was used to analyze the elemental composition, and X-ray photoelectron spectroscopy (XPS; 250xi, Thermo Scientific, USA) was used to analyze the chemical composition of the sample surface. The crystal phase of the surface was characterized using an X-ray diffractometer (XRD, D8 Focus, Bruker) equipped with a CuKα radiation source (λ = 1.54 Å) between a 2θ of 10° and 80°, the scan rate of XRD is 4°/min.

### 2.5. Cell proliferation on scaffold

After sterilization, the GU and GC samples (n = 4) were seeded with rat bone marrow mesenchymal stem cells (Lonza, Walkersville) as described previously [8]. The samples were first immersed in a culture medium for 1 h and then placed in 24-well plates (Ultra Low). A cluster plate (Costar, Corning) was added to 50 μL of culture medium containing 1 × $10^5$ cells. Dulbecco's modified Eagle's medium containing 10% FBS and 1% penicillin/streptomycin was added to the samples. The cells were cultured in an incubator at 37 °C with 5% $CO_2$, and the culture medium was refreshed twice weekly. After incubation for 3, 7, and 14 days, the viability of the cells cultured with the samples was assessed using a Cell Counting Kit (CCK-8; Dojindo, Japan). At each time point, the disks were rinsed three times in a phosphate buffered saline (PBS) solution and incubated in 10% CCK-8 solution at 37 °C for 3 h.

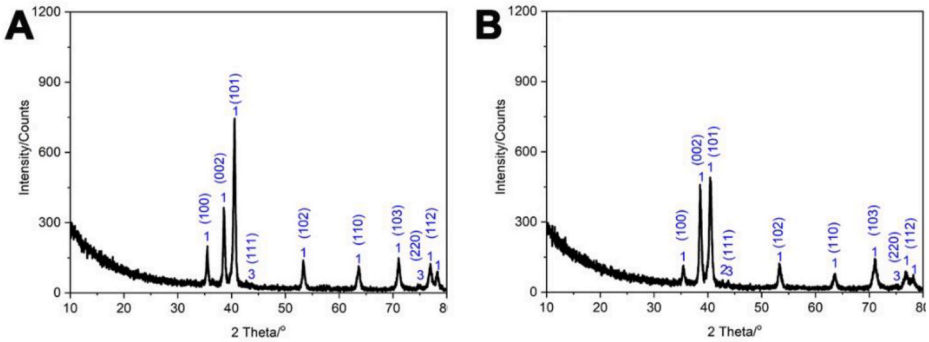


**Fig. 6.** Peak-differentiating and imitating diagram of XRD: **(A)**. GC group. **(B)**. GU group.

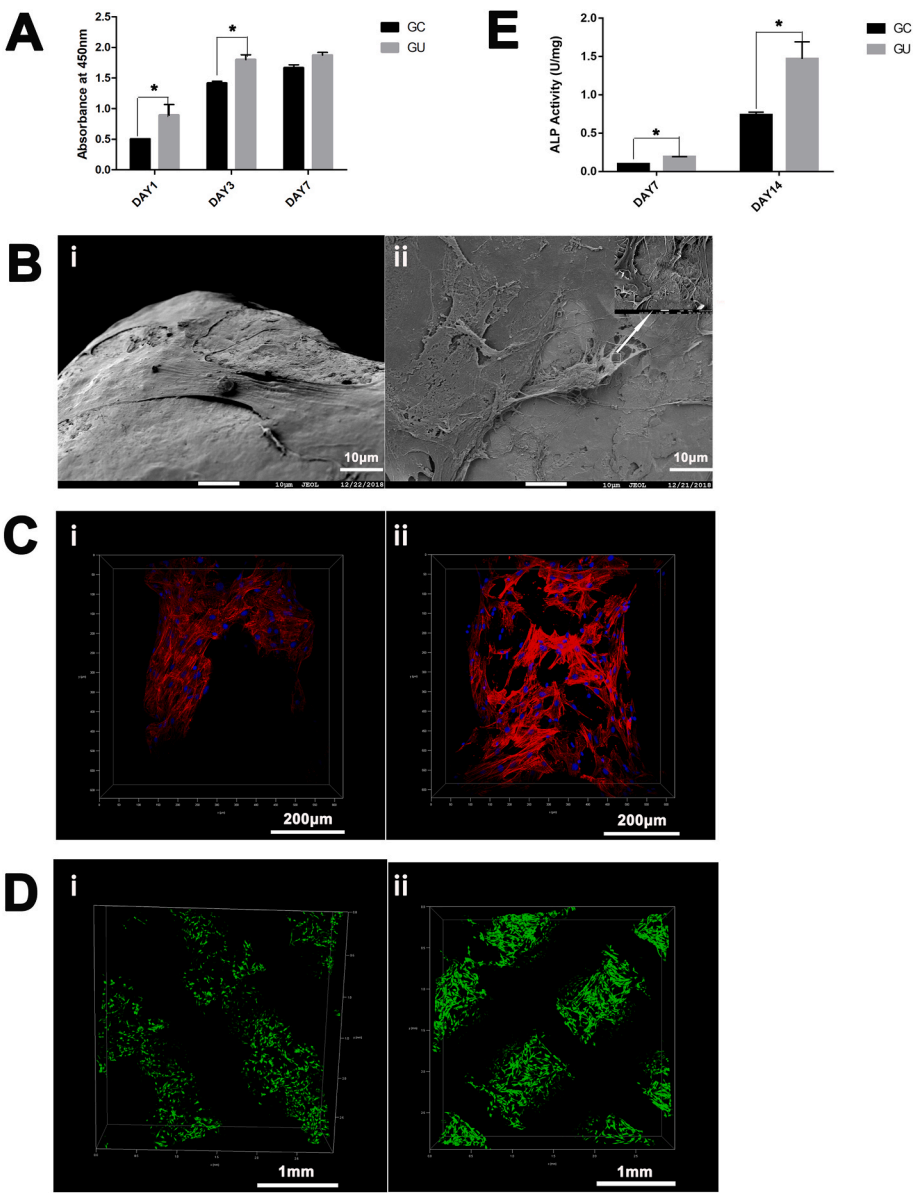


**Fig. 7.** **(A)** Rat bone marrow mesenchymal stem cell proliferation on the scaffolds of the GC and GU groups on 1, 3, and 7 days (*$p < 0.05$). **(B)** SEM observations of rat bone marrow mesenchymal stem cell proliferation on the scaffolds of the GC (i) and GU (ii) groups after 7 days of culture. **(C)** F-acting Cytoskeleton imaging of rat bone marrow mesenchymal stem cell proliferation on the scaffolds of the GC (i) and GU (ii) groups after 7 days of culture. **(D)** Live/Dead staining results of the GC (i) and GU (ii) scaffolds after 3 days of cell culture. Live and dead cells appear green and red. **(E)** ALP activity of rat bone marrow mesenchymal stem cells on the scaffolds of the GC and GU groups after 7, 14 days of culture (*$p < 0.05$).

Absorbance was measured at a 450 nm wavelength. The amount and morphology of the cells on the scaffolds were identified using a scanning electron microscope (SEM). To further investigate the cell viability on the scaffolds, we stained the live cells with calcein AM and the dead cells with propidium iodide (LIVE/DEAD cell viability kit, Dojindo) and visualized the stained samples using confocal laser scanning microscopy.

### 2.6. Alkaline phosphatase activity

Osteoblast differentiation ability was assayed *in vitro* by testing the alkaline phosphatase (ALP) activity of rat bone marrow mesenchymal stem cells. The cell culture method and seeding protocol were the same as those described above, except that the culture medium was replaced with an osteogenic medium (OM, Lonza, Walkersville) containing 0.5% ascorbate, 0.5% dexamethasone, and 1% β-glycerophosphate to induce osteogenic differentiation. After culturing the cells for 7 days, ALP activity was detected using an ALP assay kit (Beyotime, China). Cellular ALP activity was normalized to the intracellular total protein level determined using a MicroBCA protein assay kit (Pierce).

### 2.7. Mechanical test

To identify the effect of UV photofunctionalization on the compression strength of the 3D printed porous Ti6Al4V scaffolds (Ø = 10 mm, H = 5 mm, n = 5), a universal mechanics testing machine (Landmark, MTS Inc., MN, USA) was used to test the static compression before and after UV treatment. The deformation rate during compression was 1.8 mm/s, and the elastic modulus, yield strength, and compression strength were analyzed.

### 2.8. Animal surgery and fluorescent labeling

To evaluate the *in vivo* osseointegration of the porous Ti64 implants, 27 UV-treated implants and 27 untreated implants were implanted into the bilateral femur condyles of 27 healthy and mature male New Zealand rabbits. The animals were anesthetized by intramuscular injection of ketamine (50 mg/kg). The skin was sterilized with 0.5% povidone iodine, and the bilateral medial femur condyles were surgically opened. A bone defect was created using a 5 mm diameter drill under irrigation with saline, and the implant was then inserted onto the medial condyle by press fitting. The incision was closed in layers with absorbable thread

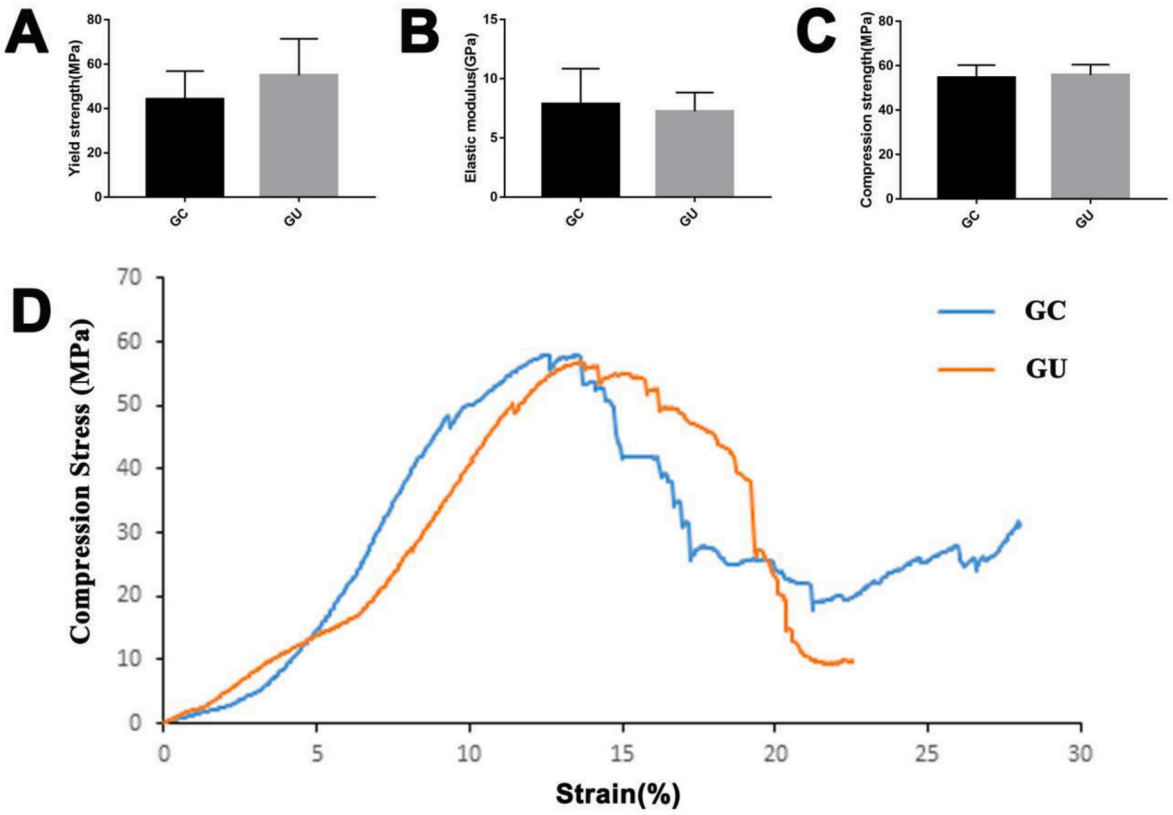


**Fig. 8.** Comparison of yield strength **(A)**, elastic modulus **(B)** and compression strength **(C)** between the GC group and GU group. **(D)**. Stress-strain curves of the GC and GU group.

(PDS II, ETHICON). Intramuscular injections of penicillin were administered at a dose of 0.1 g/kg during surgery and postoperatively for 3 days.

To determine the process of osteogenesis on the scaffold following implantation, *in vivo* sequential fluorescent labeling was performed to label the regenerated bone at different time points. Calcein green (10 mg/kg, Sigma, USA) and tetracycline (30 mg/kg, Sigma, USA) were injected subcutaneously at 3- and 7-weeks post-implantation, respectively. After 8 weeks of implantation, all animals were euthanized, and the samples with surrounding tissues were excised. The study animals were bred at the Department of Laboratory Animal Science at Peking University Health Science Center and were cared for according to the principles of the Guide for the Care and Use of Laboratory Animals, after obtaining approval from the Animal Ethics Committee of Peking University Health Science Center (approval no. LA2014214).

### 2.9. Micro-CT analysis

Six specimens from each group were scanned by micro-CT (Inveon, Siemens Medical Solutions USA, Inc.) at a scanning rate of 6°/min and a resolution of 9 μm. The X-ray source voltage was 80 kV, and the beam current was 80 mA using filtered Bremsstrahlung radiation. A 1 mm aluminum filter was used during the scanning. The micro-CT images were then reconstructed using the Inveon Acquisition Workplace. The newly grown bone was distinguished from soft tissue and metal implants by partitioning different Hounsfield units (HU). The phase of the bone was defined in the range of 1000–2250 HU. Two regions of interest (ROIs) were determined in the workstation to characterize the growth of new bone on the scaffold. They included (1) the peri-implant region at a 500 μm periphery around the scaffold and (2) the intraporous region within the scaffold. The peri-implant bone fraction was defined as the ratio of bone volume to the total volume of the region, while the intraporous bone fraction was defined as the ratio of bone volume to the total volume of the pores.

### 2.10. Histological examination

Twelve samples were retrieved for fluorescence and histological analyses at 8-weeks post-surgery. Samples were fixed in 10% formalin for 14 days and dehydrated in serial concentrations of ethanol (70%, 85%, 95%, and 100%) for 3 days. The specimens were embedded in methyl methacrylate and cut using an EXAKT system (EXAKT Apparatebau, Norderstedt, Germany). Ground sections of 40–50 μm were prepared as described previously [34].

The unstained sections from six samples of each group were analyzed under a fluorescent microscope. The bones formed at the third and seventh weeks were marked with green labels (from calcein green) and orange labels (from tetracycline), respectively. The sections from another six samples of each group were stained using the Goldner trichrome staining method, in which the implant was stained black and the cartilage purple. Osteoid, a sign of active direct bone formation, was stained orange-red, and mature mineralized bone was stained green. Quantitative analysis was performed using the Image-Pro Plus software based on two middle longitudinal sections of each block regarding the bone ingrowth (BI) and bone-implant contact ratio (BICR). Consequently, 12 slices were analyzed for each group. BI was defined as the percentage of new bone within the pores. The BICR was measured as the fraction of the surface area of the implant in contact with the bone.

### 2.11. Push-out test

A universal testing machine (Landmark, MTS Inc. MN, USA) was used to measure the push-out force between the implant and the bone. Twelve samples from each group were carefully cut at a tangential angle

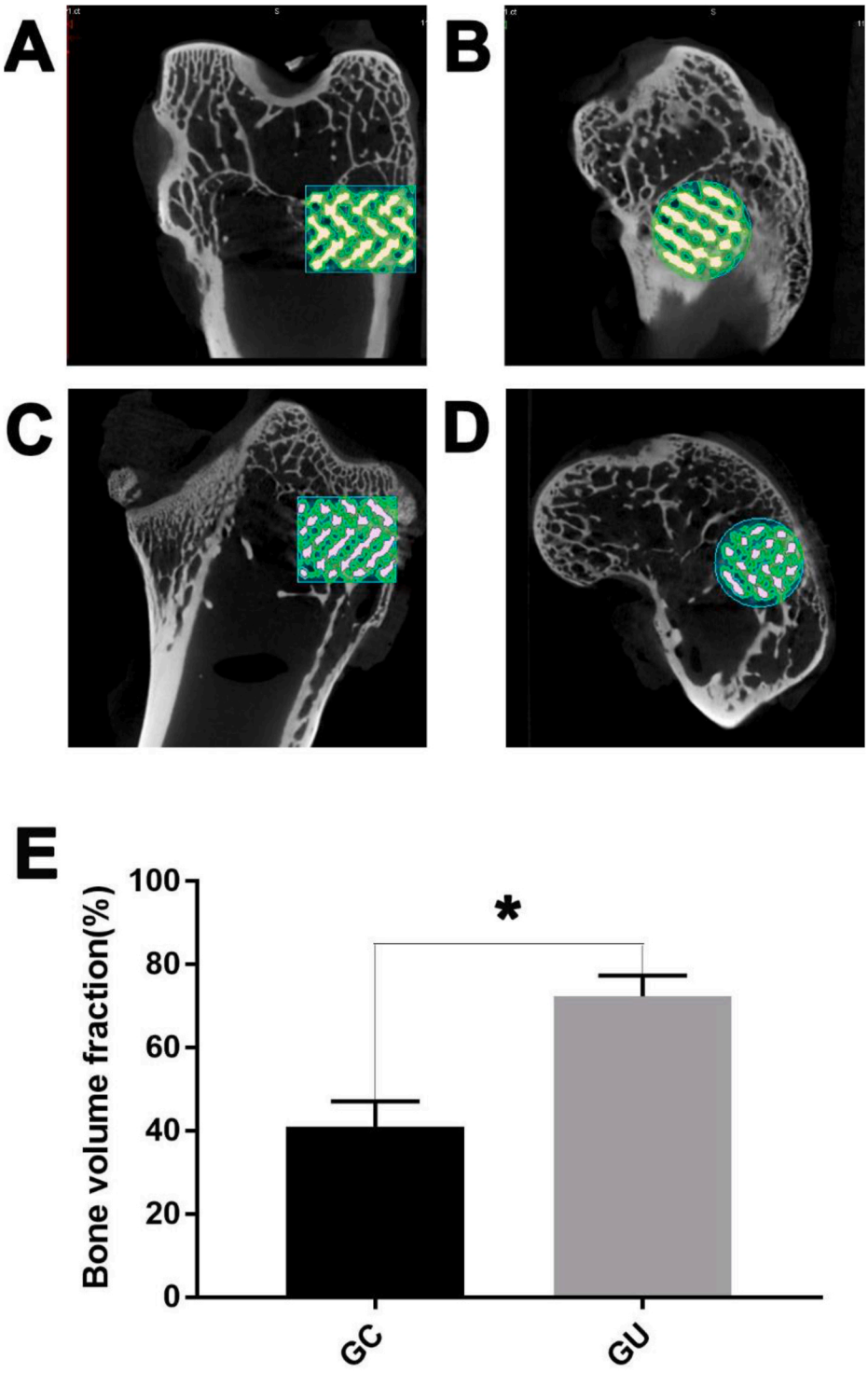


**Fig. 9.** Micro-CT images of the porous implants 8 weeks after *in vivo* implantation. Ti, bones in the peri-implant region, and those within the 3D-AVIs are labeled white, green, and pink, respectively. **(A)** Side view of the GC group. **(B)** Top view of the GC group. **(C)** Side view of the GU group. **(D)** Top view of the GU group. **(E)** Quantitative results of bone fractions in the intraporous region of the scaffolds in the GC (black) and GU (grey) groups; *$p < 0.05$ ($n = 6$ per group).

to the long axis of the implant to expose its inner side, and the periosteal bone at the outer side was removed prior to testing. A custom-designed special holder was applied to fix the sample to ensure loading alignment. The push-out procedure was then conducted at a constant rate of 1.5 mm/min. The end point of the test was the presence of an abrupt drop in the push-out force, the maximal load being documented as the push-out force.

### 2.12. Statistical analysis

For all experiments, values for statistical analysis were reported as the mean ± SD. An independent-sample *t*-test was performed to test the significant differences in the *in vitro* results, whereas the significant differences in the *in vivo* results were determined by a nonparametric test (Mann−Whitney) using SPSS (17.0 version). Statistical significance was set at $p < 0.05$.

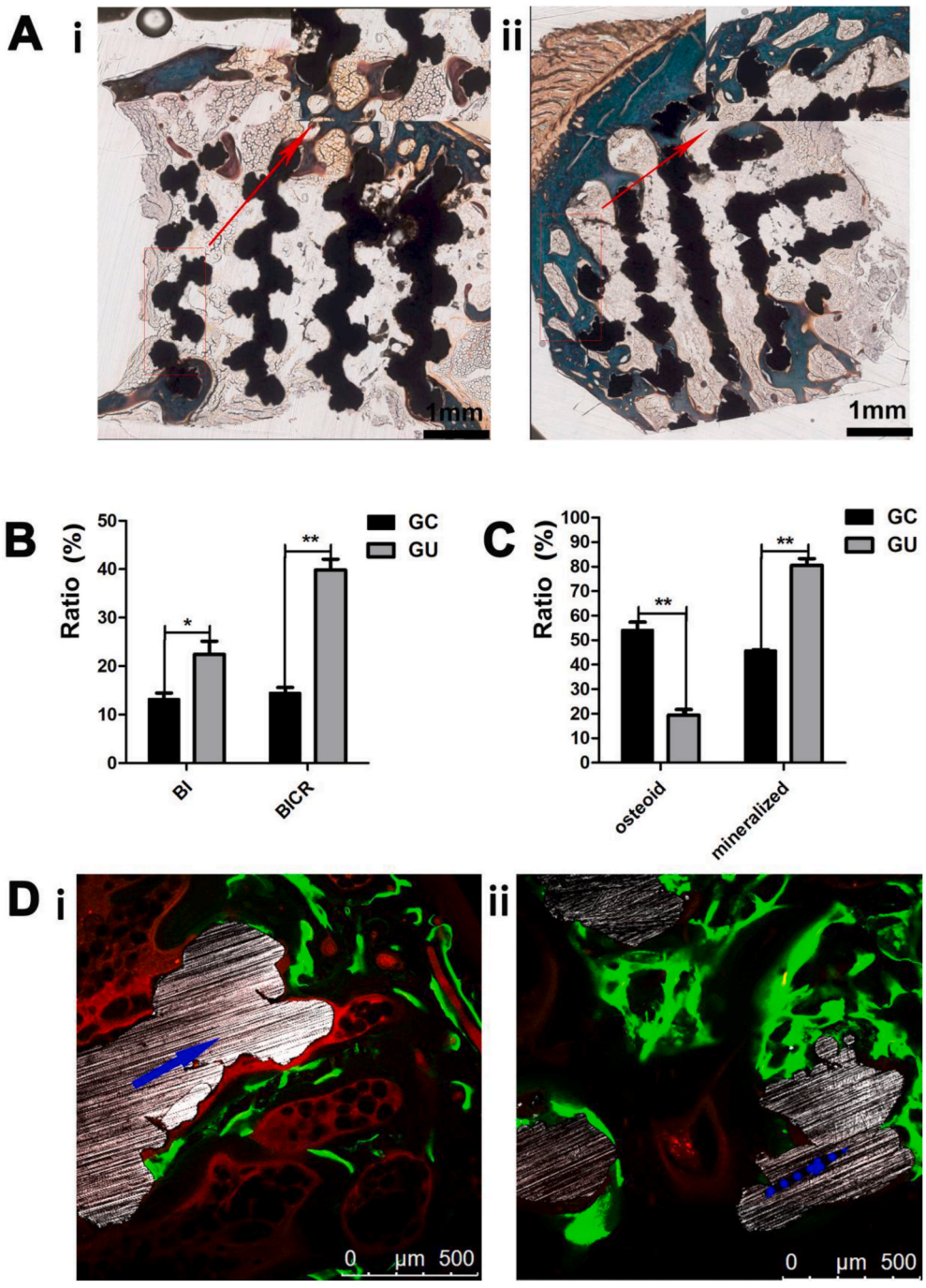


**Fig. 10. (A)** Goldner trichrome staining (representative images) of the GC(i) and GU (ii) group. **(B)** Quantitative results of the BI and BICR of the scaffolds in the GC and GU groups (n = 10). **(C)** Mineralized bone and osteoid ratios of the GC and GU groups (n = 10). **(D)** Fluorescence labeling (representative fluorescent micrographs) of the osseointegration within the pores of the scaffolds in the GC(i) and GU(ii) group (blue arrows indicate titanium struts, and green and yellow bands denote newly formed bone indicated by calcein and tetracycline, respectively).

## 3. Results

### 3.1. Hydrophilicity test

As shown in Fig. 2, the contact angle of the GU group ($\theta = 60.3° \pm 0.05°$) was significantly lower than that of the GC group ($\theta = 90.1° \pm 2.41°$) ($p < 0.05$), indicating the hydrophilicity of the GU group was significantly higher than that of the GC group in the contact angle test.

### 3.2. Physi-chemical characterization

Fig. 3 shows the changes in the surface morphology of the 3D printed titanium alloy scaffolds before and after the UV-functionalization treatment. Compared with the GC group, the microtopography of the scaffolds surface in GU group become more rough. As shown by Fig. 4, the EDS results suggest that the content of carbon (elemental C) on the inner surface of the GU group was lower than that of the GC group. Overall, the scaffolds treated with UV functionalization showed surface morphology changes and reduced C content. The chemical composition and state of the components after UV treatment were investigated by XPS, as shown in Fig. 5. Based on the survey spectrum, the major elements were O, Ti, and C. The chemical environment of the C and O elements and the relative proportions of the elements in different chemical environments were obtained and are shown in Tables 1 and 2. Three peaks could be obtained by peak-differentiating and imitating toward the narrow sweep spectrum of C elements: the corresponding binding energy of C–C, C–O, and C═O peaks were 284.82, 286.41, and 288.41 eV, respectively. Similarly, three peaks could be obtained by peak-

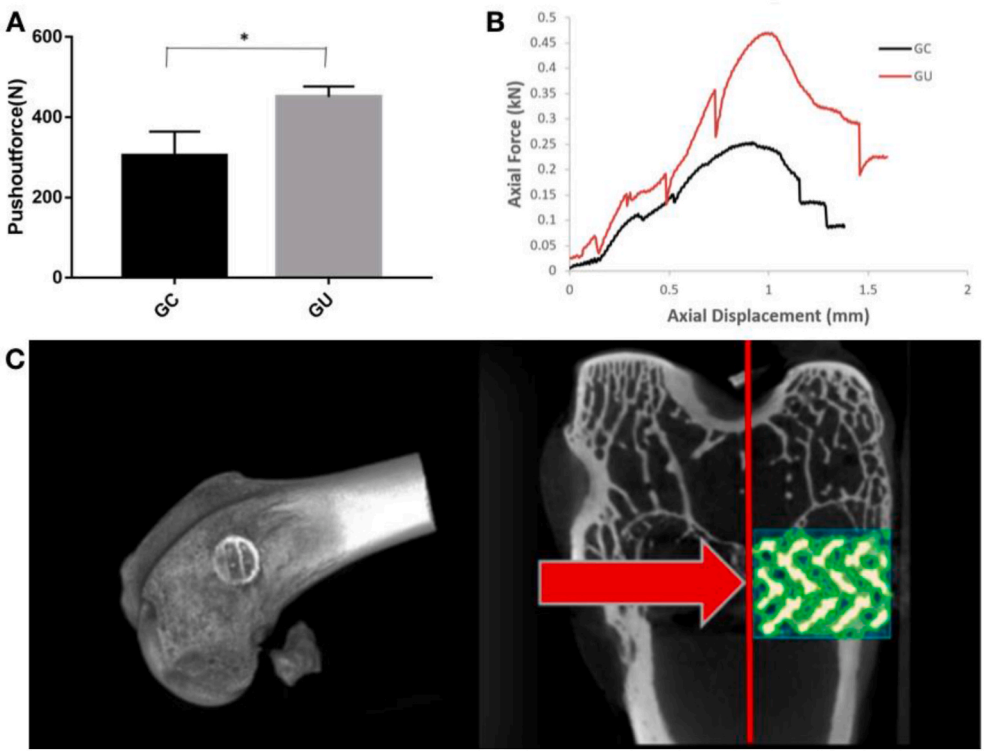


**Fig. 11.** Typical pushing-out force **(A)** and displacement curves **(B)** of the porous scaffolds following implantation for 8 weeks; *p < 0.05. **(C)** 3D Micro-CT images show the implantation site of the implant.

**Table 3**
Comparison of BI Increase Radio and BICR Increase Ratio by different Treatments.

| | Photofunctionalization | MAO [14] | BMP-2 [16] |
|---|---|---|---|
| BI Increase Ratio | 60% | 136% | 120% |
| BICR Increase Ratio | 171% | 305% | 110% |

differentiating and imitating the narrow sweep spectrum of O elements: the corresponding binding energies of the O–Ti ($TiO_2$), O–C, and O═C peaks were 529.99, 531.89, and 532.99 eV, respectively.

The results suggest that the surface of the 3D printed porous titanium alloy is composed of titanium dioxide and carbon oxide before and after the UV treatment. To reveal the phase composition of 3D printed titanium alloy scaffolds before and after UV light functionalization, XRD was performed, the results of which are shown in Fig. 6. Multiple diffraction peaks (one peak, Ti6Al4V) and a small amount of carbon (C) from the titanium matrix can be observed in both groups. Ti6Al4V was the main phase, the representative diffraction peaks being $2\theta = 35.921°$, $2\theta = 39.010°$, $2\theta = 41.166°$, $2\theta = 53.921°$, $2\theta = 64.677°$, $2\theta = 72.030°$, $2\theta = 77.923°$, and $2\theta = 79.549°$, which correspond to (200), (002), (201), (202), (220), (203), (222), and (401), respectively.

### 3.3. Cellular experiments in vitro

We evaluated the proliferation of rat bone marrow mesenchymal stem cells on the two types of scaffolds by measuring the cellular metabolic activity at different time points (1, 3, and 7 days). Our *in vitro* cell research indicated that the GU group had good cytocompatibility with rat bone marrow mesenchymal stem cells. As indicated in Fig. 7A, the GU group showed significantly better proliferative activity than the GC group ($p < 0.05$) in the first week. Next, the cell morphology on day 7 was measured by SEM and F-actin cytoskeleton imaging analysis. Under SEM, the well-stretched rat bone marrow mesenchymal stem cells on the GU group scaffolds presented filiform shapes and spread out more evenly on the substrate to form more collagen fiber attachment on the scaffold surface than the CU group (Fig. 7B). The F-actin cytoskeleton imaging analysis indicated that the rat bone marrow mesenchymal stem cells on the GU group scaffolds proliferated better and extended more pseudopodia than the CU group (Fig. 7C). Additionally, the cell viability on day 3 was measured by live/dead staining analysis (Fig. 7D). Generally, the rat bone marrow mesenchymal stem cells survived on all these scaffolds, as no dead cells (red staining) could be observed. Evidently, the cell density on the scaffolds of the GU group was higher than that of the CU group. Further, as shown in Fig. 6E, the ALP activity test showed that the GU group had higher ALP activity than the CU group at 7 and 14 days, and the difference was statistically significant ($P < 0.05$).

### 3.4. Effects of UV treatment on mechanical properties of the porous Ti6Al4V scaffolds

Fig. 8 shows a comparison of the mechanical properties (yield strength, elastic modulus, compression strength) between the GC and GU group scaffolds, there being no significant difference between them ($p > 0.05$).

### 3.5. Micro-CT analysis

To explore the effect of UV photofunctionalization on the *in vivo* osseointegration of the porous scaffolds, we quantified bone formation within it using micro-CT analysis. As shown in Fig. 9A, B, 9C, and 9D, the Ti alloy and bones within the scaffolds were labeled white and green, respectively. Overall, the GU group showed more bone formation. The quantitative analysis results of the bone fraction in the intraporous region of the porous implants are shown in Fig. 9E. Compared with the GC group (40.52 ± 6.59%), the bone fraction in the intraporous region was significantly higher in the GU group (71.53 ± 5.63%) ($p < 0.05$). Consequently, UV photofunctionalization enhanced BI into porous

scaffolds.

### 3.6. Histologic analysis

Representative histological images revealed the integration between the newly formed bone tissue and the Ti alloy surface in the two groups (Fig. 10A and B). Quantitative measurements of mineralized bone, osteoid, and BI in the ROIs confirmed the histomorphological findings. Fig. 10C shows a significantly higher BI (*$p < 0.05$) and BICR (**$p < 0.01$) at the implants in the GU group than in the GC group. As indicated in Fig. 10D, the mineralized bone ratio was significantly higher in the GU group than in the GC group (**$p < 0.01$). Furthermore, fluorescence labeling indicated that osteogenesis occurred earlier in the GU group (mostly at 3 weeks) than in the GC group (mostly at 8 weeks).

### 3.7. Biological fixation strength

Fig. 11Bshows typical displacement curves during the push-out tests. It was found that the UV photofunctionalization scaffolds had a steeper curve than the GC group, demonstrating that they required a higher force to generate a similar displacement. Fig. 11A shows a comparison of the push-out forces between the two groups. It was calculated that the push-out force for the GC group was approximately 304.7 ± 29.75 N, and it was enhanced to 450.5 ± 18.5 N after UV treatment ($p < 0.05$).

## 4. Discussion

Prior studies have documented various methods to enhance the osseointegration of 3D-printed porous Ti6Al4V implants. However, these methods have several insurmountable disadvantages such as their high costs, extra surgical trauma, complicated preparation process with a long preparation time or the reduction of the mechanical strength of the scaffolds[ [27] [28]]. In this study, a special device was designed for the UV treatment of 3D-printed porous Ti6Al4V implants, which was proved to be a simple and effective approach to improve osseointegration. The major findings of this study were as follows: (1) the specially designed UV photofunctionalization device was effective in improving the osseointegration of 3D-printed porous Ti6Al4V implants *in vivo*, and the scaffold surface exhibited better cytocompatibility after UV treatment. (2) The UV treatment could increase the hydrophilicity and reduce the contamination of carbon on the scaffold surface while preserving the original mechanical properties of the porous titanium alloy scaffolds.

UV photofunctionalization is mainly used in dental clinic to treat traditional nonporous dental implants for enhancing bone-to-implant contact [18,24]. However, few studies have applied UV photofunctionalization to the porous implants of orthopedics, the reason for which lies in the blocking of UV rays by the porous structure. Hence, to guarantee that the surface of the porous implant can be evenly treated, an omnidirectional radiator was created.

As indicated by Fig. 3, more rough topographic surface was obtained after UV treatment. After searching the literature database, we found that the topographic change for 3D printed porous Ti6Al4V scaffolds after UV treatment had not been studied before [33,34]. It was demonstrated that the rougher topographic surface was more favorable to osseointegration of the Ti6Al4V implant [35]. The EDS analysis indicated that the carbon element on the surface decreased after UV treatment, which is consistent with other studies [31,36–38]. The decreased atomic carbon was due to the photocatalytic phenomena of titanium dioxide [39]. Moreover, Hydrophilicity test showed that the hydrophobic surface of the untreated Ti6Al4V became superhydrophilic after UV treatment. Before UV treatment, the titanium surface showed hydrophobicity and the water droplet remained without spreading, The contact angle between water droplet and titanium surface before UV treatment is 60.3° ± 0.05°, In contrast, in the UV treatment group, the water droplet spread on the titanium surface with a contact angle of 90.1° ± 2.41°. The increased hydrophilicity could promote protein adsorption on the titanium surface. It is reported that the amount of albumin and fibronectin on UV photofunctionalized titanium surface were remarkably greater than on untreated titanium surface, suggesting that UV is benificial for the titanium surface to absorb cells and proteins [40]. On a photofunctionalized titanium surface, all osteoblast activities such as proliferation, differentiation, and mineralization are enhanced *in vitro* [39,41,42]. Aita et al. [39] reported that the level of hydrocarbon strongly correlated with the rates of protein adsorption and cell attachment. They also reported that the level of protein adsorption and the number of cells attached to control titanium surfaces remained low compared with those on UV-treated surfaces [39]. These findings indicate that the amount of hydrocarbon on the Ti6Al4V surface is crucial in determining the initial affinity level for osteoblasts, consequently dominating the degree of osseointegration *in vivo*. Bone tissue engineering, especially the 3D printed porous Ti6Al4V implants, still poses challenges such as an insufficient supply of osteogenic cells for bone formation [43–45]. The results of the present study have shown that our omnidirectional radiator endow the 3D printed porous Ti6Al4V implants enhanced osteoconductivity through more bone regeneration and more mature of the newly formed bone.

Biological aging of titanium is related to a decrease in hydrophilicity and progressive contamination with hydrocarbons [21,22,41,42], which slows the cellular response, decreases the bone-implant contact rate by up to 50%, and greatly reduces the biomechanical resistance of implants [30,39]. The results of the hydrophilicity test and physiochemical characterization in this study revealed that UV treatment could increase the hydrophilicity and reduce the carbon contamination of the scaffold surface significantly, leading to an increase in the BICR and biological fixation strength. Decontamination also leads to increased adhesion of organic and cellular components [42,48,49], resulting in increased bone formation. The reason why UV can reduce carbon contamination lies in the UV energy can break the bonds between Ti5c atoms and the O and/or N atoms of contaminant molecules. Hence, the chemically active Ti5c sites become available for the attachment to O, N, S atoms present in any protein, leading to improved biocompatibility of the implant [20]. The hydrophilicity increase mainly attribute to the carbon concentration decrease [39,41]; And another important reason is that UV (270 nm) irradiation could decrease the amount of $H_2O$ and increase the amount of Ti–OH. Moreover, UV induces a one-electron oxidation with water to produce a hydroxyl radical OH and dissociation of H. These hydroxyl groups together with the O-Vacancies present on an the carbon free surface are able to form more OH groups [20,46,47]. In particular, no other methods, such as acid pickling or microarc oxidation [14], with the same mechanism as UV photofunctionalization has been found till now.

The fluorescence labeling results of the present study showed that the osteogenesis of scaffolds occurred earlier after UV treatment (3 vs. 7 weeks), demonstrating that UV photofunctionalization can shorten healing time while conveniently improving the prognosis. Thus, it may be extremely useful in certain clinical situations, especially those involving low primary stability or patients with systemic diseases requiring emergency operations [50–55]. Micro-CT analysis showed that the newly formed bone on untreated scaffolds was thinner than that on the UV-treated scaffolds. The difference between untreated and UV-treated implants was more evident in the histological analysis. The BI and BICR of the UV-treated group were significantly higher than those of the untreated group. By contrast, the mineralized/osteoid bone ratio of the UV-treated group was significantly higher than that of the untreated group, resulting in greater bone-implant integration strength, as shown by the push-out test results. The presence of more cortical bone emphasized the effect of UV photofunctionalization on bone formation on the Ti alloy surfaces. UV photofunctionalization has been reported to attract or recruit osteogenic cells to Ti surfaces and more bone tissue in the vicinity of the Ti implant [22,38], which is consistent with the experimental results of this study. Ueno et al. also reported that UV

photofunctionalization enhanced ALP activity and mineralization in periosteal cells [32].

The present study did have several limitations. First, we made our observations at 8 weeks after surgery, which could be considered a medium-term observation time—that is, no long-term observation was completed in this study. Secondly, in our study, 270 and 365 nm UV led beads were used for 15 min treatment. It is possible that we may have achieved different results using different UV led beads for a longer or shorter irradiation times. Thirdly, after making a quantitative comparison with other surface treatments methods for 3D printed porous Ti6Al4V implants (Table 3), we found that the BI increase ratio needs to be further improved. Finally, a clinical trial of the efficacy of UV-treated 3D-printed porous Ti6Al4V implants when applied to patients is expected in the near future.

## 5. Conclusions

In this work, we successfully designed an omnidirectional radiator based on ultraviolet photofunctionalization for the customized surface treatment of the 3D-printed porous Ti6Al4V implants. It can be concluded that 1) the present method can significantly improve the hydrophilicity($90.1^\circ \pm 2.41^\circ$ vs $60.3^\circ \pm 0.05^\circ$) and ALP activity($0.68 \pm 0.08$ U/mg vs $1.47 \pm 0.25$U/mg) of the porous Ti6Al4V implants while reducing the carbon contamination (65.84% vs 48.06%) in the surface, 2) that the present method can enhance osteoinetegration of porous Ti6Al4V scaffolds via increasing BI ($13.84\% \pm 1.41\%$ vs $22.16\% \pm 2.49\%$), BICR ($14.66\% \pm 1.38\%$ vs $39.76\% \pm 2.27\%$), mineralized bone ratio ($43.66\% \pm 1.38\%$ vs $79.86\% \pm 3.37\%$) and osteoid bone ratio ($53.66\% \pm 3.38\%$ vs $19.87\% \pm 2.87\%$). 3) that the present method can evenly treat the surface of the porous implants while preserving its original macro morphology, and 4) that the present method is easy to operate with a low cost.

## Funding

The authors acknowledge the grant from the Ministry of Science and Technology of the People's Republic of China (grant number 2016YFB1101501) and Beijing Municipal Science & Technology Commission (Project Z181100001718195). Teng Zhang was supported in part by the Postdoctoral Fellowship of Peking-Tsinghua Center for Life Sciences. We also received research and financial support from the Beijing AKEC Medical Co., Ltd.

## Author contributions

Chuan Yin and Zhongjun Liu designed the study. Zhongjun Liu and Hong Cai supervised the project. Teng Zhang, Qingguang Wei and Peng Xiu conducted the animal surgeries and most of the animal experiments. Huijie Leng conducted the three-point bending tests and finite element analysis. Yun Tian and Yan Cheng analyzed the results. Caimei Wang and Jian Li designed and fabricated the scaffolds. Teng Zhang prepared the manuscript. Shiqing Feng revised the manuscript.

## Data and materials availability

All data associated with this study are present in the paper.

## Declaration of competing interest

None.

## References

[1] A. Nauth, E. Schemitsch, B. Norris, Z. Nollin, J.T. Watson, Critical-size bone defects: is there a consensus for diagnosis and treatment? J. Orthop. Trauma 32 (2018) S7–S11, https://doi.org/10.1097/BOT.0000000000001115.

[2] M. Gage, F. Liporace, K. Egol, T. McLaurin, Management of bone defects in orthopedic trauma, Bull. Hosp. Jt. Dis. 76 (2018) 4–8.

[3] P.V. Giannoudis, H. Dinopoulos, E. Tsiridis, Bone substitutes: an update, Injury 36 (Supplement 3) (2005) S20–S27, https://doi.org/10.1016/j.injury.2005.07.029.

[4] T. Zhang, Q. Wei, H. Zhou, Z. Jing, X. Liu, Y. Zheng, H. Cai, F. Wei, L. Jiang, M. Yu, Y. Cheng, D. Fan, W. Zhou, X. Lin, H. Leng, J. Li, X. Li, C. Wang, Y. Tian, Z. Liu, Three-dimensional-printed individualized porous implants: a new "implant-bone" interface fusion concept for large bone defect treatment, Bioact. Mater. 6 (2021) 3659–3670, https://doi.org/10.1016/j.bioactmat.2021.03.030.

[5] T. Ji, Y. Yang, X. Tang, H. Liang, T. Yan, R. Yang, W. Guo, 3D-Printed modular hemipelvic endoprosthetic reconstruction following periacetabular tumor resection: early results of 80 consecutive cases, J. Bone. Joint. Surg. Am. 102 (2020) 1530–1541, https://doi.org/10.2106/JBJS.19.01437.

[6] A. Cheng, D.J. Cohen, A. Kahn, R.M. Clohessy, K. Sahingur, J.B. Newton, S.L. Hyzy, B.D. Boyan, Z. Schwartz, Laser sintered porous Ti-6Al-4V implants stimulate vertical bone growth, Ann. Biomed. Eng. 45 (2017) 2025–2035, https://doi.org/10.1007/s10439-017-1831-7.

[7] P. Sapienza, L. Di Marzo, A. Cucina, C. Burchi, V. Corvino, A. Mingoli, A. Cavallaro, High-porosity and normal-porosity prostheses. Differences in growth factor release, Minerva Cardioangiol. 46 (1998) 141–148.

[8] M.C. Kennady, M.R. Tucker, G.E. Lester, M.J. Buckley, Stress shielding effect of rigid internal fixation plates on mandibular bone grafts. A photon absorption densitometry and quantitative computerized tomographic evaluation, Int. J. Oral Maxillofac. Surg. 18 (1989) 307–310, https://doi.org/10.1016/s0901-5027(89)80101-8.

[9] R. Maity, S. Majumder, A. Roychowdhury, S. Saha, Effect of plate geometry modifications to reduce stress shielding during healing stages for tibial fracture fixation, J. Long Term Eff. Med. Implants 28 (2018) 131–140.

[10] H. Minamikawa, T. Ikeda, W. Att, Y. Hagiwara, M. Hirota, M. Tabuchi, H. Aita, W. Park, T. Ogawa, J. Biomed. Mater. Res. A 102 (2014) 3618–3630, https://doi.org/10.1615/JLongTermEffMedImplants.2018027269.

[11] J.C. Melville, N.N. Nassari, I.A. Hanna, J.W. Shum, M.E. Wong, S. Young, Immediate transoral allogeneic bone grafting for large mandibular defects. Less morbidity, more bone. A paradigm in benign tumor mandibular reconstruction? J. Oral Maxillofac. Surg. 75 (2017) 828–838, https://doi.org/10.1016/j.joms.2016.09.049.

[12] R. Verboket, M. Leiblein, C. Seebach, C. Nau, M. Janko, M. Bellen, H. Bönig, D. Henrich, I. Marzi, Autologous cell-based therapy for treatment of large bone defects: from bench to bedside, Eur. J. Trauma Emerg. Surg. 44 (2018) 649–665, https://doi.org/10.1007/s00068-018-0906-y.

[13] Y. Watanabe, N. Harada, K. Sato, S. Abe, K. Yamanaka, T. Matushita, Stem cell therapy: is there a future for reconstruction of large bone defects? Injury 47 (2016) S47–S51, https://doi.org/10.1016/S0020-1383(16)30012-2.

[14] P. Xiu, Z. Jia, J. Lv, C. Yin, Y. Cheng, K. Zhang, C. Song, H. Leng, Y. Zheng, H. Cai, Z. Liu, Tailored surface treatment of 3D printed porous Ti6Al4V by microarc oxidation for enhanced osseointegration via optimized bone in-growth patterns and interlocked bone/implant interface, ACS Appl. Mater. Interfaces 8 (2016) 17964–17975, https://doi.org/10.1021/acsami.6b05893.

[15] J.P. Govindharajulu, X. Chen, Y. Li, J.C. Rodriguez- Cabello, M. Battacharya, C. Aparicio, Chitosan-recombinamer layer-by-layer coatings for multifunctional implants, Int. J. Mol. Sci. 18 (2017) 369, https://doi.org/10.3390/ijms18020369.

[16] T. Zhang, Q. Wei, D. Fan, X. Liu, W. Li, C. Song, Y. Tian, H. Cai, Y. Zheng, Z. Liu, Improved osseointegration with rhBMP-2 intraoperatively loaded in a specifically designed 3D-printed porous Ti6Al4V vertebral implant, Biomater. Sci. 8 (2020) 1279–1289, https://doi.org/10.1039/C9BM01655D.

[17] H. Tominaga, K. Matsuyama, Y. Morimoto, T. Yamamoto, S. Komiya, Y. Ishidou, The effect of ultraviolet photofunctionalization of titanium instrumentation in lumbar fusion: a non-randomized controlled trial, BMC Muscoskel. Disord. 20 (2019) 292, https://doi.org/10.1186/s12891-019-2672-3.

[18] C. Mehl, M. Kern, F. Neumann, T. Bähr, J. Wiltfang, V. Gassling, Effect of ultraviolet photofunctionalization of dental titanium implants on osseointegration, J. Zhejiang Univ. - Sci. B. 19 (2018) 525–534, https://doi.org/10.1631/jzus.B1600505.

[19] M. Hirota, T. Ikeda, M. Tabuchi, T. Ozawa, I. Tohnai, T. Ogawa, Effects of ultraviolet photofunctionalization on bone augmentation and integration capabilities of titanium mesh and implants, Int. J. Oral Maxillofac. Implants 32 (2017) 52–62, https://doi.org/10.11607/jomi.4891.

[20] M. Roy, A. Pompella, J. Kubacki, J. Szade, R.A. Roy, W. Hedzelek, Photofunctionalization of titanium: an alternative explanation of its chemical-physical mechanism, PloS One 11 (2016), e0157481, https://doi.org/10.1371/journal.pone.0157481.

[21] N. Hori, W. Att, T. Ueno, N. Sato, M. Yamada, L. Saruwatari, T. Suzuki, T. Ogawa, Age-dependent degradation of the protein adsorption capacity of titanium, J. Dent. Res. 88 (2009) 663–667, https://doi.org/10.1177/0022034509339567.

[22] F. Iwasa, N. Hori, T. Ueno, H. Minamikawa, M. Yamada, T. Ogawa, Enhancement of osteoblast adhesion to UV-photofunctionalized titanium via an electrostatic mechanism, Biomaterials 31 (2010) 2717–2727, https://doi.org/10.1016/j.biomaterials.2009.12.024.

[23] N. Hori, T. Ueno, H. Minamikawa, F. Iwasa, F. Yoshino, K. Kimoto, M.C. Lee, T. Ogawa, Electrostatic control of protein adsorption on UV-photofunctionalized titanium, Acta Biomater. 6 (2010) 4175–4180, https://doi.org/10.1016/j.actbio.2010.05.006.

[24] M. Hirota, T. Ozawa, T. Iwai, K. Mitsudo, T. Ogawa, UV-mediated photofunctionalization of dental implant: a seven-year results of a prospective study, J. Clin. Med. 9 (2020) 2733, https://doi.org/10.3390/jcm9092733.

[25] T.D. Cutler, J.J. Zimmerman, Ultraviolet irradiation and the mechanisms underlying its inactivation of infectious agents, Anim. Health Res. Rev. 12 (2011) 15–23, https://doi.org/10.1017/S1466252311000016.
[26] K.M. Hosamani, K.S. Katagi, Characterization and structure elucidation of 12-hydroxyoctadec-cis-9-enoic acid in Jatropha gossypifolia and Hevea brasiliensis seed oils: a rich source of hydroxy fatty acid, Chem. Phys. Lipids 152 (2008) 9–12, https://doi.org/10.1016/j.chemphyslip.2007.11.003.
[27] C. Vaquette, N. Bock, P.A. Tran, Layered antimicrobial selenium nanoparticle-calcium phosphate coating on 3D printed scaffolds enhanced bone formation in critical size defects, ACS Appl. Mater. Interfaces 12 (2020) 55638–55648, https://doi.org/10.1021/acsami.0c17017.
[28] J. Lv, P. Xiu, J. Tan, Z. Jia, H. Cai, Z. Liu, Enhanced angiogenesis and osteogenesis in critical bone defects by the controlled release of bmp-2 and vegf: implantation of electron beam melting-fabricated porous Ti6al4v scaffolds incorporating growth factor-doped fibrin glue, Biomed. Mater. 10 (2015), 035013.
[29] T. Ogawa, Ultraviolet photofunctionalization of titanium implants, Int. J. Oral Maxillofac. Implants 29 (2014) e95–102, https://doi.org/10.11607/jomi.te47.
[30] F. Iwasa, K. Baba, T. Ogawa, Enhanced intracellular signaling pathway in osteoblasts on ultraviolet lighttreated hydrophilic titanium, Biomed. Res. 37 (2016) 1–11, https://doi.org/10.2220/biomedres.37.1.
[31] N. Arroyo-Lamas, U. Ugalde, I. Arteagoitia, Decontamination of Ti oxide surfaces by using ultraviolet light: Hg-vapor vs. LED-based irradiation, Antibodies 9 (2020) 11, https://doi.org/10.3390/antibiotics9110724.
[32] T. Ueno, M. Yamada, T. Suzuki, H. Minamikawa, N. Sato, N. Hori, K. Takeuchi, M. Hattori, T.O. Arteagoitia, Enhancement of bone-titanium integration profile with UV-photofunctionalized titanium in a gap healing model, Biomedica 31 (2010) 1546–1557, https://doi.org/10.1016/j.
[33] Naoko Ikeo, Takuya Ishimoto, Hidetsugu Fukuda, Takayoshi Nakano, Fabrication and characterization of porous implant products with aligned pores by EBM method for biomedical application, Adv.Mat.Res. 409 (2011) 142–145. https://doi.org/10.4028/www.scientific.net/AMR.409.142.
[34] Y. Cao, M. Delin, F. Kullenberg, L. Nyborg, Surface modification of Ti-6Al-4V powder during recycling in EBM process, 52, https://doi.org/10.1002/sia.6847, 2020, 1066-1070.
[35] Y. Miyamoto, K. Fujisawa, T. Sumitomo, T. Yuasa, Effect of surface topography on osseointegration establishment of dental implant comparison between smooth and rough surfaces, 52, https://doi.org/10.11237/jsoi.17.216, 2004, 216-226.
[36] M. Yamada, T. Miyauchi, A. Yamamoto, F. Iwasa, M. Takeuchi, M. Anpo, K. Sakurai, Enhancement of adhesion strength and cellular stiffness of osteoblasts on mirror-polished titanium surface by UV-photofunctionalization, Acta Biomed. 6 (2010) 4578–4588, https://doi.org/10.1016/j.actbio.2010.07.010.
[37] W. Att, N. Hori, F. Iwasa, M. Yamada, T. Ueno, T. Ogawa, The effect of UV-photofunctionalization on the time-related bioactivity of titanium and chromium–cobalt alloys, Biomedica 30 (2009) 4268–4276, https://doi.org/10.1016/j.biomaterials.2009.04.048.
[38] T. Miyauchi, M. Yamada, A. Yamamoto, F. Iwasa, T. Suzawa, R. Kamijo, K. Baba, T. Ogawa, The enhanced characteristics of osteoblast adhesion to photofunctionalized nanoscale TiO2 layers on biomaterials surfaces, Biomedica 31 (2010) 3827–3839, https://doi.org/10.1016/j.biomaterials.2010.01.133.
[39] H. Aita, N. Hori, M. Takeuchi, T. Suzuki, M. Yamada, M. Anpo, T. Ogawa, The effect of ultraviolet functionalization of titanium on integration with bone, Biomaterials 30 (2009) 1015–1025, https://doi.org/10.1016/j.biomaterials.2008.11.004.
[40] Z. Qin, W. Teng, Effect of ultraviolet-photofunctionalization of titanium on protein adsorption and competition 50 (2015) 428–432.
[41] Wael Att, N. Hori, M. Takeuchi, J. Ouyang, Y. Yang, M. Anpo, T. Ogawa, Time-dependent degradation of titanium osteoconductivity: an implication of biological aging of implant materials, Biomaterials 30 (2009) 5352–5363, https://doi.org/10.1016/j.biomaterials.2009.06.040.
[42] W. Att, T. Ogawa, Biological aging of implant surfaces and their restoration with ultraviolet light treatment: a novel understanding of osseointegration, Int. J. Oral Maxillofac. Implants 27 (2012) 753–761.
[43] D. Flanagan Photofunctionalization of Dental Implants, J. Oral Implantol. 42 (2016) 445–450, https://doi.org/10.1563/aaid-joi-D-15-00145.
[44] S. Razzouk, R. Schoor, Mesenchymal stem cells and their challenges for bone regeneration and osseointegration, J. Oral Implantol. 83 (2012) 547–550, https://doi.org/10.1902/jop.2011.110384.
[45] P. Sreejit, R.S. Verma, Natural ECM as biomaterial for scaffold based cardiac regeneration using adult bone marrow derived stem cells, St.Cel Rev. Rep. 9 (2013) 158–171, https://doi.org/10.1007/s12015-013-9427-6.
[46] B.N. CaM, Principles of $TiO_2$ photocatalysis, in: Y. Ohama, D. Van Gemert (Eds.), Applications of Titanium Dioxide Photocatalysis to Construction Materials, Springer Netherlands, 2011, pp. 5–10.
[47] S.G. Steinemann, Titanium—the material of choice? Per 17 (1998) (2000) 7–21, https://doi.org/10.1111/j.1600-0757.1998.tb00119.x.
[48] G. Zhao, Z. Schwartz, M. Wieland, F. Rupp, J. Geis-Gerstorfer, D.L. Cochran, B. D. Boyan, High surface energy enhances cell response to titanium substrate microstructure, J. Biomed. Mater. Res. A 74 (2005) 49–58, https://doi.org/10.1002/jbm.a.30320.
[49] J. Shen, Y. Chen, G. Yang, X. Wan, F. He, H. Wang, Effects of storage medium and UV photofunctionalization on time-related changes of titanium surface characteristics and biocompatibility, J. Biomed. Mater. Res. B 104 (2016) 932–940, https://doi.org/10.1002/jbm.b.33437.
[50] S. Suzuki, H. Kobayashi, T. Ogawa, Implant stability change and osseointegration speed of immediately loaded photofunctionalized implants, Implant Dent. 22 (2013) 481–490, https://doi.org/10.1097/ID.0b013e31829deb62.
[51] Y. Sugita, Y. Honda, I. Kato, K. Kubo, H. Maeda, T. Ogawa, Role of photofunctionalization in mitigating impaired osseointegration associated with type 2 diabetes in rats, Int. J. Oral Maxillofac. Implants 29 (2014) 1293–1300, https://doi.org/10.11607/jomi.3480.
[52] M. Ishijima, A. Ghassemi, P. Soltanzadeh, M. Tanaka, K. Nakhaei, W. Park, M. Hirota, N. Tsukimura, T. Ogawa, Effect of UV photofunctionalization on osseointegration in aged rats, Implant Dent. 25 (2016) 744–750, https://doi.org/10.1097/ID.0000000000000459.
[53] M. Hirota, T. Ozawa, T. Iwai, T. Ogawa, I. Tohnai, Implant stability development of photofunctionalized implants placed in regular and complex cases: a case-control study, Int. J. Oral Maxillofac. Implants 31 (2016) 676–686, https://doi.org/10.11607/jomi.4115.
[54] H. Kitajima, T. Ogawa, The use of photofunctionalized implants for low or extremely low primary stability cases, Int. J. Oral Maxillofac. Implants 31 (2016) 439–447, https://doi.org/10.11607/jomi.4054.
[55] M. Kim, H. Choi, J. Lee, J. Kim, H. Jung, J. Kim, Y. Park, H. Moon, UV photofunctionalization effect on bone graft in critical one-wall defect around implant: a pilot study in beagle dogs, BioMed Res. Int. 31 (2016) 4385279, https://doi.org/10.1155/2016/4385279.